Partial Regrowth of Optical-Gain Section for Improved Wafer Process Flexibility of InP Photonic Integrated Circuits

Yuta Ueda, *Member, IEEE*, Yusuke Saito, Josuke Ozaki, Yoshihiro Ogiso, *Member, IEEE*, Takahiko Shindo, *Member, IEEE*, Yasuaki Hashizume, and Mitsuteru Ishikawa, *Member, IEEE*

***Abstract*—We developed a semiconductor regrowth scheme for InP photonic integrated circuits (PICs) with optical-gain sections. Unlike conventional semiconductor regrowth schemes, a limited area corresponding to a 200-μm waveguide of an original epitaxial wafer is replaced with an optical-gain material, which improves the flexibility of a PIC process design. In this paper, we describe the partial regrowth (PRG) procedure using a window regrowth mask that defines the regrowth area. A minimum window in terms of semiconductor quality assurance is determined by observing the micro-photoluminescence intensities of the replaced regions. We also show basic performances of optical semiconductor amplifiers (SOAs) obtained by the PRG including amplification of in-phase/quadrature modulation optical signals. Furthermore, practical InP PIC applications of the PRG are also depicted: an SOA-integrated Mach-Zehnder modulator and an electrooptically tunable laser with an arrayed gain.**

***Index Terms*—Mach-Zehnder modulator, photonic integrated circuits, semiconductor growth, semiconductor optical amplifier, tunable laser.**

I. Introduction

PHOTONIC integrated circuits (PICs) are key for compact, cost-effective, and low-power dissipation optical components for optical communication and sensing systems since the number of components (lens, fiber, package) are minimized and connection losses among optical functions are reduced. [1], [2] Although there are some PIC platforms such as silica [3] and silicon photonics [4], [5], InP PICs are superior due to their better optical-gain function, higher electrooptic efficiency (intensity/phase modulator), and higher responsivity (photo detector) [6]. A feature of an InP PIC fabrication is semiconductor regrowth on an original epitaxial wafer to integrate different material properties such as the bandgap, which makes the PIC multifunctional. Fig. 1 shows a common semiconductor regrowth scheme of an InP PIC. Once a first epitaxial wafer (1st epi) is grown, it is removed except for "island" areas covered with hard masks. After the removal, a 2nd epi is grown on the original wafer. For example, when we consider an electro-absorption modulator (EAM) integrated laser [7]–[11], known as an industry successful InP PIC, the 1st and 2nd epi commonly correspond to the laser and EAM section, respectively.

An essential point of the regrowth process is that the width of the island area is limited to be less than a few tens of μm to suppress the increase in the growth rate (degradation of the wafer flatness, resulting in a poor accuracy of the photolithographic process) and/or the semiconductor composition fluctuation (e.g., bandgap shift) in the vicinity of the hard mask. Therefore, the 1st epi area (island area) in the conventional regrowth scheme is applied only to stripe-type devices such as an EAM. In other words, when it comes to non-stripe-type devices that occupy plane areas on a wafer such as cascaded space optical switches [12], nested Mach-Zehnder modulators (MZMs) [13]–[15], and arrayed gain sections [16], it is difficult to apply the conventional regrowth scheme.

The limitation of the conventional regrowth causes the low wafer process flexibility of InP PICs. Fig. 2 shows a fabrication process of an in-phase/quadrature modulator (IQM) based on nested-MZMs with a semiconductor optical amplifier (SOA) [17]. When we fabricate an SOA-integrated IQM (SOA-IQM), the 1st epi consists of a multi-quantum well (MQW) with an optical gain (Fig. 2(a)). Next, we replace the SOA-MQW with the electrooptic (EO) MQW for the phase modulation function. Then, the overclad growth is implemented. Finally, the waveguide structure is formed by the photolithographic process. On the other hand, the 1st epi for an IQM without SOA (basic IQM) corresponds to Fig. 2(b) except for an SOA section. Therefore, we need to prepare different 1st epis for an SOA-IQM and a basic IQM, which increases the wafer cost (unavailable for mass production effect) and/or causes the low wafer process compatibility between two types of PICs. Using the same 1st epi is also important, especially when the quality control of the 1st epi is difficult. For example, while aluminum (Al) material is used in the MQW of an IQM for a high EO efficiency [15], the quality of the Al-MQW is sensitive to the growth condition such as oxygen background. [18] Therefore, ensuring the same performances of PICs made of Al-MQWs grown as 1st and 2nd epi causes the process management costs to further increase.

Manuscript received October 4, 2021; revised November 12, 2021; accepted December 13, 2021. Date of publication December 20, 2021; date of current version April 18, 2022. *(Corresponding author: Yuta Ueda.)*

The authors are with the NTT Device Innovation Center, Nippon Telegraph and Telephone Corporation, Atsugi, Kanagawa 243-0007, Japan (e-mail: yuta.ueda.dh@hco.ntt.co.jp; yusuke.saito.kn@hco.ntt.co.jp; josuke.ozaki.mp@hco.ntt.co.jp; yoshihiro.ogiso.uv@hco.ntt.co.jp; takahiko.shindo.xu@hco.ntt.co.jp; yasuaki.hashizume.ph@hco.ntt.co.jp; mitsuteru.ishikawa.pe@hco.ntt.co.jp).

Color versions of one or more figures in this article are available at https://doi.org/10.1109/JLT.2021.3136814.

Digital Object Identifier 10.1109/JLT.2021.3136814

This work is licensed under a Creative Commons Attribution-NonCommercial-NoDerivatives 4.0 License. For more information, see https://creativecommons.org/licenses/by-nc-nd/4.0/

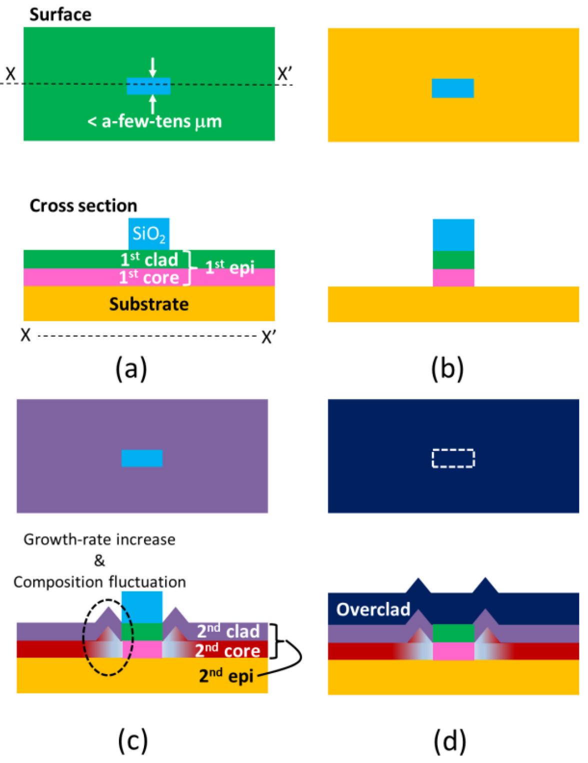

Fig. 1. Schematic of conventional regrowth process for stripe-type PIC. Top: Wafer surface, Bottom: Cross section. (a) Formed "island" mask on original wafer with 1st epi. (b) 1st epi removal except for island area. (c) Semiconductor regrowth for 2nd epi.. (d) Overclad growth.

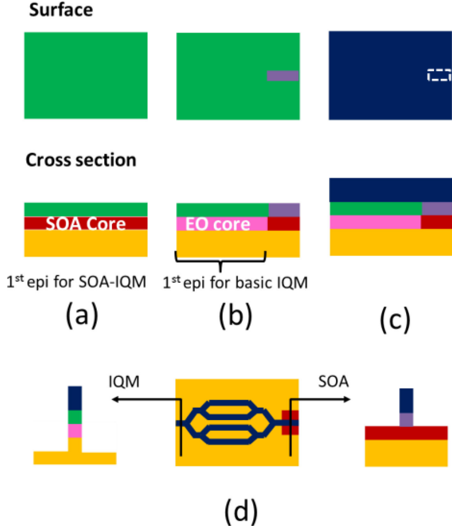

Fig. 2. Schematic of wafer process of (SOA-integrated) IQM by conventional regrowth process. (a) 1st epi with SOA core. (b) Semiconductor regrowth for EO core. (c) Photographic-process-ready wafer after overclad growth (d) Waveguide structure of SOA-IQM.

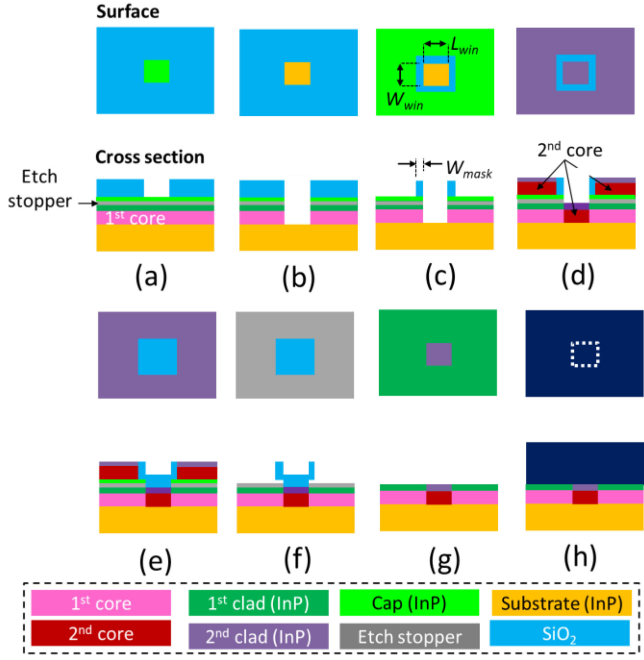

Fig. 3. Schematic of PRG. (a) "Window" mask formed on 1st epi. (b) 1st epi removal inside window mask. (c) Removing window mask (d) Semiconductor regrowth for 2nd epi. (e) Hard mask on regrowth area. (f) Removing 2nd epi outside hard mask using etch stopper. (g) Removing etch stopper and hard mask. (h) Overclad growth.

The above problems can be solved if we can use the 1st epi with the EO-MQW rather than the SOA-MQW, which means that we need to partially replace the former with the latter.

In this paper, we describe a newly developed partial regrowth (PRG) process for InP PICs in which only limited areas on a 1st epi are *replaced* with the 2nd epi while stripe areas are *preserved* in the conventional regrowth. We successfully replaced a limited area corresponding to a 200-μm waveguide of a 1st epi with an EO-MQW with a 2nd one with an SOA-MQW. An SOA fabricated using the PRG exhibits practical optical amplification for an IQ-modulation optical signal. Furthermore, we also show applications of the PRG involving an SOA-integrated dual-polarization IQM (SOA-DP-IQM) and a tunable laser with an arrayed gain section.

II. Mask Design of PRG

Fig. 3 shows the PRG procedure. In the PRG, it is preferable to introduce an InP cap (<100 nm) and an InGaAsP etch stopper (<100 nm) on the 1st epi which is useful in 2nd-epi removal described latter. First, we form a SiO_2 "window mask" on a 1st epi (Fig. 3(a)). When a target PIC does not need regrowth, overclad growth is immediately implemented after removing the cap and the etch stopper. Next, the 1st epi inside the window mask is removed by an etching process (Fig. 3(b)) and the window mask is further processed as shown in Fig. 3(c). Then, semiconductor regrowth by metal-organic chemical vapor deposition (MO-CVD) is implemented to fill the removed area with a 2nd epi (Fig. 3(d)). The MO-CVD condition (700 °C, 75 torr) is not optimized for the regrowth process and we can adjust the 2nd-epi quality only by the window-mask design described below. After the 2nd epi regrowth, the window mask is removed and a new SiO_2 layer is deposited. The SiO_2 layer is processed so that it masks the partially regrowth region (Fig. 3(e)). The excess 2nd

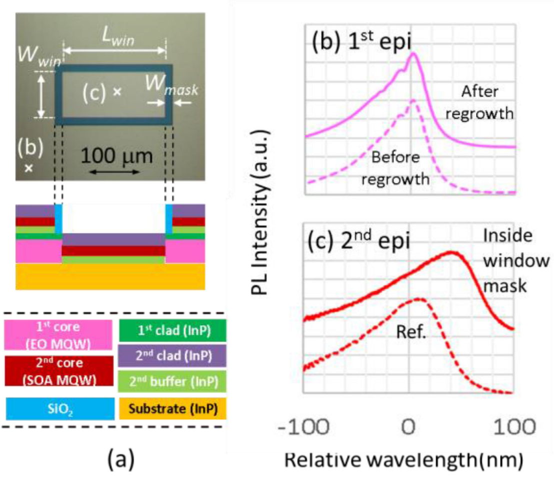

Fig. 4. (a) Photograph (top) and corresponding cross-sectional schematic (bottom) of PRG wafer after 2nd-epi growth. (b) μ-PL spectra of 1st epi (outside window mask) before and after regrowth. (c) μ-PL spectra of 2nd epi (inside window mask) and reference epi grown on a bare wafer. Window-mask parameters for the spectrum "inside widow mask" shown in (c): W_{mask}, W_{win}, $L_{win} = 15, 60, 100$ μm.

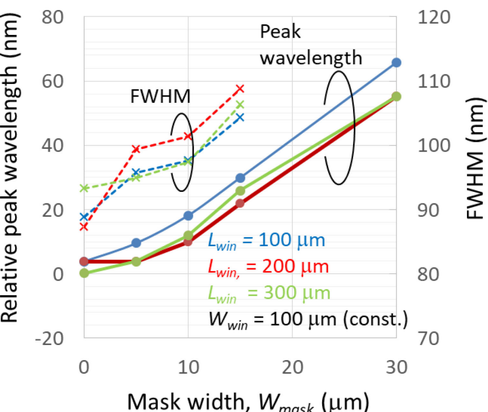

Fig. 5. Peak wavelength and FWHM of μ-PL spectrum as a function of W_{mask}.

epi outside the hard mask (regrowth region) is removed by wet etching using the etch stopper (Fig. 3(f)) and the residual etch stopper and hard mask are also stripped (Fig. 3(g)). The cap and the etch stopper are useful when a buffer InP under the 2nd core (under clad) is needed to be completely removed. Finally, an overclad layer is grown (Fig. 3(h)).

A key to establishing the PRG is the window-mask width (W_{mask}) that determines the wafer flatness and/or the semiconductor quality as described in the introduction. In addition to W_{mask}, the dimension of the inside-edge of the window (W_{win} and L_{win} as indicated in Fig. 3(c)) is also important since these define the 2nd-epi area. To experimentally clarify criteria for the mask dimensions, we prepared window masks with various W_{mask}, W_{win}, and L_{win} on a 1st epi which is composed of an InAlGaAs MQW (500 nm) and InP (150 nm) grown on an InP substrate. No etch stopper (Fig. 3) is introduced to simplify the procedure in the experiment. We also implemented the PRG on the 1st epi by MO-CVD. The 2nd epi of the PRG consists of InP buffer (150 nm), InAlGaAs MQW (270 nm), and InP clad (230 nm). The total thickness (650 nm) corresponds to the total one of the 1st epi described above. The target photoluminescence (PL) of the MQW in the 2nd epi is set to 1.55-μm-band optical amplification. Fig. 4(a) shows a photograph (top) and a corresponding cross-sectional schematic (bottom) of the PRG wafer after 2nd-epi growth. Fig. 4(b) displays micro-PL (μ-PL) spectra of the 1st epi before and after the regrowth of the 2nd epi outside the window mask [indicated in Fig. 4(a)]. We confirmed no change of characteristics of the 1st-epi MQW after the regrowth. Fig. 4(c) shows a μ-PL spectrum measured at a center inside the window mask (indicated in Fig. 4(a)) whose W_{mask}, W_{win}, and L_{win} are 15, 60, and 100 μm, respectively. A reference spectrum measured from the same 2nd epi grown on a bare wafer (no hard mask) is also shown. We observed a red shift of μ-PL spectrum from inside the window mask. The red shift is caused by a higher semiconductor-growth rate due to MO material migration on the hard mask [19], resulting in the grown MQW having a thicker well layer than the designed MQW. In addition to the thicker well thickness of the MQW, the μ-PL peak shift is also induced by the material composition fluctuation and the resulting strain effect of the MQW, which derives from the MO-material dependence of the migration length. While the increase in the growth rate in vicinity of a hard mask reaches a scale of 100% (twice growth rate), the MO-material dependence of the increase is typically $\sim$10 points [20], [21]. This means that the contribution of the composition fluctuation to the μ-PL peak shift is limited ($\sim$10% of the total shift in general for practical growth condition) compared to that of a thicker-well layer. Fig. 5 shows peak wavelengths and full-width half maximums (FWHMs) of the μ-PL spectra inside window mask as a function of W_{mask}. In the figure, $W_{mask} = 0$ μm corresponds to no hard mask. As W_{mask} increases, both the peak wavelength and the FWHM increase due to enhanced MO- material migration on a wider hard mask. While some reasons are possible for the increase in the FWHM such as degradation of the well/barrier boundary sharpness, we estimate the main cause of the broadening is the spatial resolution of the μ-PL ($\sim$1 μm) and the planarly fluctuated MQW in the vicinity of the hard mask. It is found that L_{win} has little effect on the μ-PL peak wavelengths and the FWHMs for L_{win}>100 μm, which indicates that we can fabricate an SOA shorter than 200 μm in the PRG if we use an appropriate W_{mask}. The minimum size is small enough for a practical SOA as described in section II.

To directly observe the influence of the window mask on the growth rate in the PRG, we obtained sectional scanning electron microscope (SEM) images of the PRG wafer (Fig. 6). As understood from Fig. 6(a), when $W_{mask} = 0$ μm (no hard mask), it is difficult to separately remove the excess 2nd epi whose corresponding process step is shown in Fig. 3(f). Fig. 6(b) shows that the migration material on the hard mask is successfully consumed to fill the side-etched 1st core. Thus, there is little significant increase in the growth rate. The roughness at the regrowth boundary is $\sim$100 nm, which is allowable for following an overclad growth and a photolithographic process to define a PIC structure. The side-etch depth of the 1st core depends on the

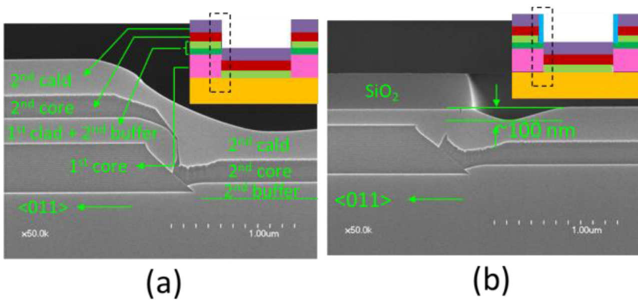

Fig. 6. Cross-sectional SEM images after 2nd-epi growth. (a) $W_{mask} = 0$ μm (no hard mask). (b) $W_{mask} = 10$ μm.

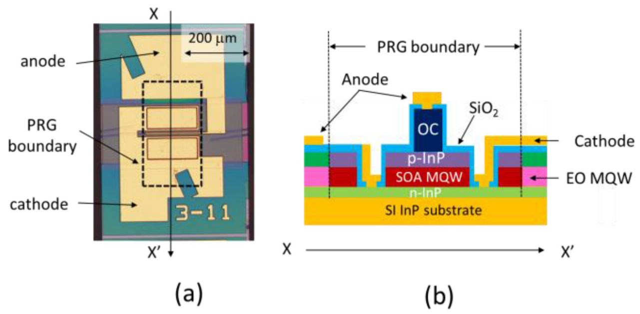

Fig. 7. (a) Photograph of SOA chip fabricated by PRG. (b) Cross-sectional schematic.

wet-etching time for 1st core removal. So, a thick 1st core results in a deep side-etch that affects the flatness of the wafer after PRG. This is the same limitation for the 1st epi as a conventional regrowth process.

From experimental results shown in Figs. 5 and 6, we determined $W_{mask} = 10$ μm to balance between the MQW quality and the process tolerance. Although the above results may vary depending on the regrowth temperature and/or pressure (migration length of MO materials), the experimental procedure and discussion are useful to determine the window-mask dimension of PRG.

III. Fundamental Performance of SOA Obtained by PRG

An application of PRG is SOA integration in a non-stripe-type PIC such as an SOA-IQM as mentioned in the introduction. To prove the practical performance of SOAs fabricated by the PRG, we made SOAs from a 1st epi with an EO-MQW and a 2nd epi with an SOA-MQW. A photograph and schematic are shown in Fig. 7. The waveguide is a ridge structure, and anti-refraction coatings are formed at both the input and output facets. Since the SOA is fabricated on a semi-insulating (SI) substrate, cathode electrodes are installed at both sides of the ridge waveguide. As indicated in Fig. 7(a), a limited 1st-epi area (200 μm $\times$ 400 μm in the case in Fig. 7(a)) is replaced with the 2nd epi. In this section, we discuss optical amplification performances for coherent signals of SOAs fabricated by the PRG.

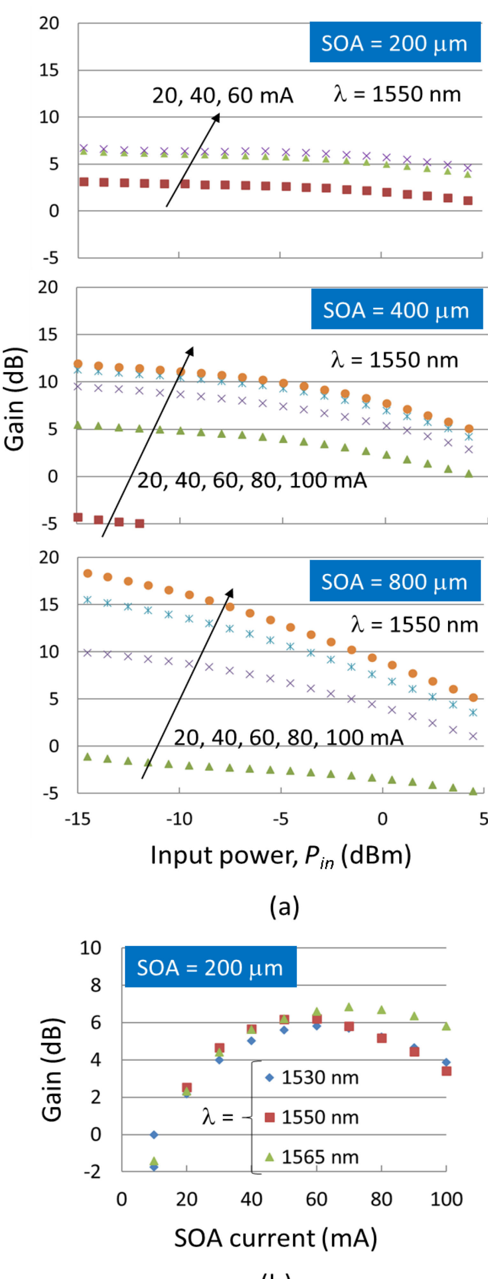

Fig. 8. (a) Static gain of SOAs (200, 400, 800 μm) as a function of input power for input wavelength of 1550 nm. (b) Wavelength dependence of 200-μm SOA for $P_{in} = -4$ dBm.

A. Basic Performance of SOA Fabricated by PRG

We measured the static optical-gain performance of SOAs with lengths of 200, 400, and 800 μm that were fabricated by the PRG with corresponding L_{win}. Fig. 8(a) shows the optical net gains of the SOAs as a function of input power (P_{in}) for an input light wavelength (λ) of 1550 nm. In all experiments in this paper, including the one in Fig. 8, the SOA chip temperature was set at 45 °C. The input light was from a commercially available tunable laser with a signal-to-spontaneous emission ratio of ~60 dB and polarized into the TE-mode with a polarization

controller. Lensed fibers are used for input and output light. P_{in} is obtained by subtracting the coupling loss between the lensed fiber and the SOA input facet from the laser output. The optical gain is defined as P_{out}/P_{in}. Here, P_{out} is the SOA-output power excluding SOA-fiber coupling loss. Even for an SOA with 200-μm, over 5-dB optical net gain including the wavelength dependence (Fig. 8(b)) is obtained in the linear region (a flat-gain region for $P_{in} < \sim$+0 dBm), which is practical for a post SOA in an IQM [17]. Note that the obtained net gain includes losses caused by optical scattering and/or absorption at the PRG boundary between the 1st and 2nd epi (Fig. 6). While measurement methods for precisely determining the loss and/or the reflectance at regrowth boundaries such as observing amplified-spontaneous-emission spectral ripples are reported [22], we have measured performances of Fabry–Pérot lasers with/without regrowth boundary. As a result, we have roughly estimated the loss to be less than 0.5 dB at one boundary. Although detailed reflectance is not obtained for the PRG boundary, our tunable laser fabricated by the PRG shows practical tuning performance (section IV.B) whose lasing mode selectivity is generally affected by the reflection at the boundary.

It is obvious that a longer SOA is beneficial to a larger optical gain because of a longer light-MQW interaction length and a lower thermal roll-off as observed in Fig. 8(b). Meanwhile, the P_{in} dependence of the optical gain was found to become significant for a longer SOA as observed in Fig. 8(a). The non-linear effect derives from the carrier consumption due to a high-photon density in the SOA and leads to optical signal distortions of outputs [23], [24]. Thus, practical SOAs need to balance the net gain and the non-linear effect.

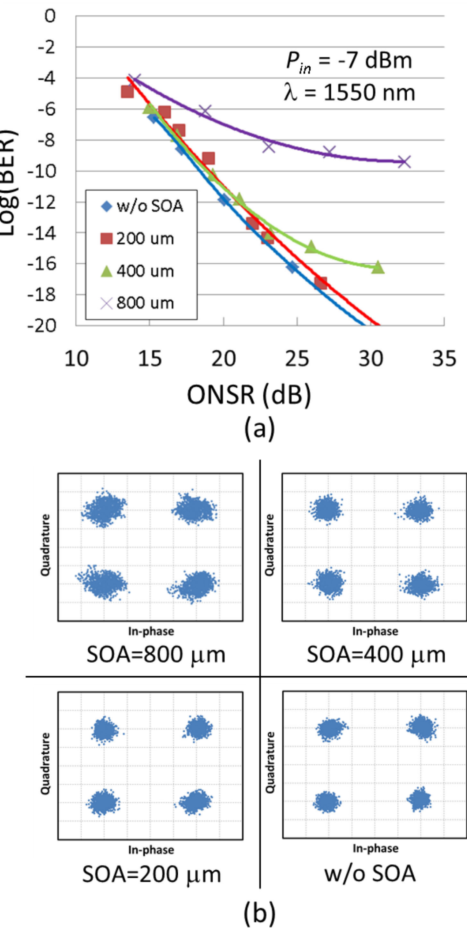

Fig. 9. (a) BER of 32Gbaud QPSK signals from SOAs (200, 400, and 800 μm) a function of OSNR, (b) corresponding constellation maps for OSNR = 30 dB.

B. Optical Amplification of IQ-Modulation Signals

Fig. 9(a) displays a set of bit-error rate (BER), estimated by the error vector magnitude of constellation maps, as a function of the optical signal-to-noise ratio (OSNR). We chose 32-Gbaud quadrature-phase shift keying (QPSK) optical signals, which is a mature format in 100G coherent systems, while higher baud-rate formats have been discussed recently. Since the response speed of the SOA non-linear effect is typically ∼1 GHz determined by the free-carrier lifetime, using such a low baud rate is a strict evaluation. P_{in} was set to −7 dBm (under modulation), which corresponded to +∼0 dBm after amplification when the maximum gain of our SOA with 200 μm (Fig. 8(a)) is applied. In the experiment, currents into SOAs were chosen to be 60, 100, and 100 mA for 200-, 400-, and 800-μm SOAs, respectively, so that the optical gain was maximum for each SOA. When we see BER $= 1 \times 10^{-12}$, the OSNR penalty due to the SOA is less than 1 dB. Since there is little penalty difference between BERs of the 200- and 400-μm SOA, 400-μm is the optimal length of our SOA in terms of the balance between the optical gain and the non-linear effect.

When we focus on the BER of the SOA with 800 μm, we find an error floor at BER = $\sim 10^{-9}$. Fig. 9(b) shows consecration maps corresponding to OSNR = ∼30 dB in Fig. 9(a). For the SOA of 800 μm, there is larger intensity and phase noise in the constellation map compared with other results. We believe that this is due to the non-linear effect of the SOA. Specifically, optical signals are distorted by the non-linear effect, which means the carrier density dynamically changes in the SOA, resulting in the refractive index fluctuation (phase noise). Note that for a given output power, we can reduce P_{in} when we use a long SOA as far as a required OSNR is achieved, which is effective to suppress the non-linear effect. Fig. 10 shows the P_{in} dependence of BER of our 800-μm SOA. We found that the non-linear effect can be suppressed by reducing P_{in}. When $P_{in} = -13$ dBm (corresponding $Po = \sim$+3 dBm from Fig. 8(a)), BER$<10^{-12}$. The important fact is that we achieve the OSNR>30 dB even for such a small P_{in}, which indicates the internal loss of our SOA fabricated by PRG is low enough to ensure practical noise figure.

From the above discussion, it is clarified that while an SOA of 200-μm length is a minimum dimension in the PRG and has an optical gain larger than 5 dB, we can use a 400-μm (or longer for a smaller P_{in}) SOA with >10-dB gain and the suppressed non-linear effect. The result indicates that the PRG is beneficial for a simple wafer process for non-stripe-type PICs with practical active functions.

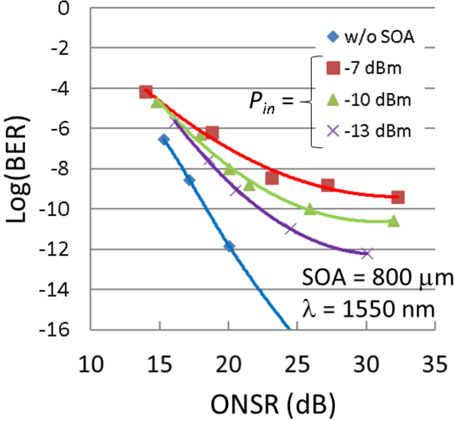

Fig. 10. P_{in} dependence of BER of 800-μm SOA.

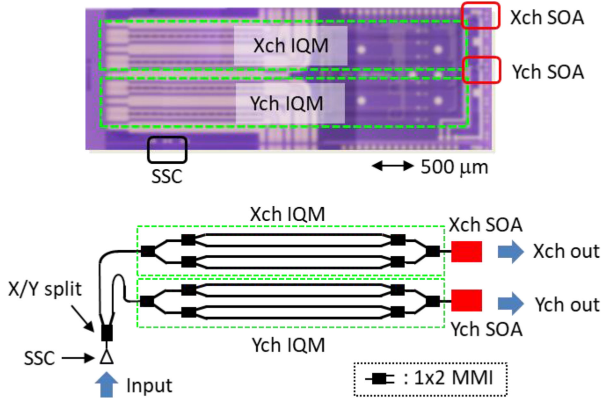

Fig. 11. Photograph and schematic of SOA-DP-IQM.

IV. Applications of PRG

In this section, we show two kinds of non-stripe-type PICs with active gain sections fabricated by the PRG.

A. SOA-DP-IQM

A DP-IQM is a typical non-stripe-type InP PIC, and the wafer process compatibility between DP-IQMs with and without SOA is an issue when the production line needs to cover both types as discussed in the introduction. We applied the PRG to the fabrication process of an SOA-DP-IQM (Fig. 11) to use the same 1st epi as our conventional DP-IQM without SOA [25]. Specifically, we start the wafer process with a 1st epi with an EO-MQW and partially replace it with a 2nd one with an SOA-MQW. To keep the original DP-IQM performance, we employed the same doping profile in the overclad growth step of the PRG (Fig. 3(h)). This means that the overclad is optimized for the DP-IQM rather than integrated SOAs. The SOA-DP-IQM consists of four MZMs. Each MZM consists of two 1 $\times$ 2 multi-mode interference couplers (MMIs) and two arm waveguides on which capacitively loaded traveling-wave electrodes are formed. The PIC has a spot-size converter (SSC) at the input port that has a thinner core layer than other PIC areas. The fabrication process of the SSC described in our previous

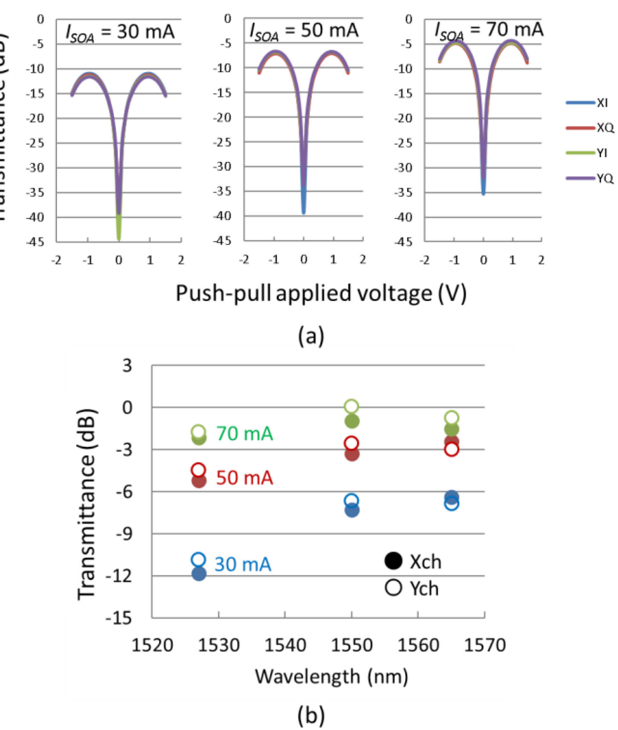

Fig. 12. SOA-DP-IQM performances. (a) Extinction curves as a function of push-pull voltage. (b) Wavelength dependence of insertion loss.

report [29] is compatible with the PRG which needs no change of the original epi (EO MQW). SOAs are integrated at the two IQM outputs for the X and Y polarization channels (Xch and Ych). The SOA-MQW and the waveguide structure are the same as ones described in section III. The lengths of SOAs are chosen to be 300 μm to balance between the net gain and non-linear effect as also discussed in section III.

Fig. 12(a) displays static extinction curves as a function of push-pull voltage for MZM electrodes for SOA currents of 30, 50, and 70 mA. One MZM from XI, XQ, YI, and YQ was operated while other MZMs were set to the off state. The input light wavelength and polarization were 1550 nm and TE-mode, respectively. Bias voltages to MZM arms were adjusted ($-$8.5V) so that differential half-wave voltages (V_π) were 1.9 V. It should be noted that the bias voltages of $-$8.5V for $V_\pi = 1.9$V (wavelength = 1550 nm) are comparable to a bias voltage of a DP-IQM without SOA. This is thanks to the same EO-MQW of the SOA-DP-IQM as that of an original DP-IQM. Furthermore, the overclad-doping profile is not changed, which results in the comparable depletion-layer thickness (affected by the p-dopant diffusion from the overclad) between two types of DP-IQM.

We coupled +7 dBm optical power into the PIC through the SSC. The total loss before an SOA for each polarization channel was assumed to be $\sim$14 dB including a fundamental loss caused by XY splitting (3 dB) and an IQ splitting and coupling (3 dB + 3 dB). The residual 5 dB was caused by the EO bias (1 dB) and the propagation loss (4 dB) in the PIC waveguide (e.g., MMI excess loss). Therefore, the input power into each SOA was about $-$7 dBm. We found over 25-dB extinction ratios (ERs) of the four

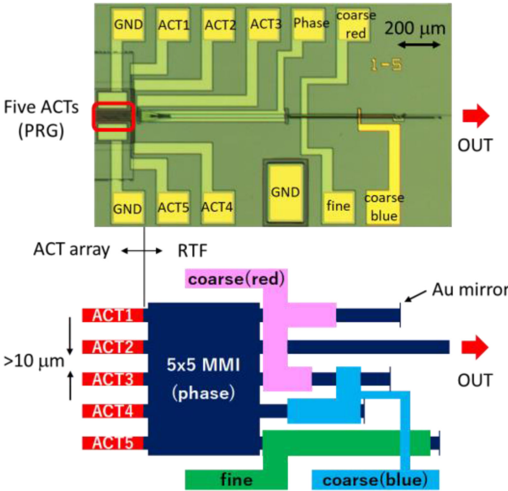

Fig. 13. Photograph and schematic of RTF laser with ACT array.

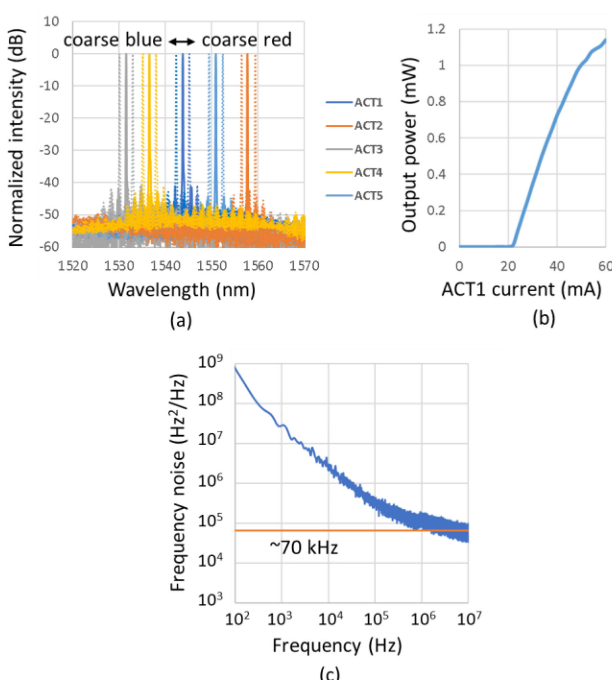

Fig. 14. RTF laser performances. (a) Lasing spectra of RTF laser: Spectra plotted with dashed line are obtained by applying voltages to coarse red and blue tuning electrodes shown in Fig. 13. (b) Output power as a function of injection current into ACT1. (c) Frequency noise spectrum when ACT1 was biased (40 mA).

MZMs. While a larger transmittance was obtained for a larger SOA current, the ERs were successfully kept at over 25 dB. This indicates that SOAs fabricated by the PRG has no defect at the regrowth boundary between the SOA and the EO-MQW that causes unintended excitation of higher propagation modes and/or optical reflection.

We also evaluated the practical optical amplification including the wavelength dependence as shown in Fig. 12(b). In the figure, the transmittances were defined as ones measured when all MZMs were on-state and each IQM for each polarization channel was set to the quadrature state (3-dB loss). Therefore, the fundamental loss was 6 dB including XY splitting (3 dB), resulting in the total loss of 11 dB. We achieved about –2 dB transmittance when SOA current was 70 mA, which corresponds to 0-dB loss (loss less) after polarization multiplexing with a 1-dB assembling loss. The result also proves that we successfully controlled the wavelength dependence of SOA (bang gap) fabricated even in limited regrowth areas in the PRG discussed in Fig. 5.

B. Arrayed Gain Section of Tunable Laser

An arrayed gain is commonly used for a tunable laser or multi-light source [27] PIC in which an operation wavelength band is shared by each active gain section (ACT). Here we show an application of the PRG to an electrooptically tunable reflection-transversal filter (RTF) laser with an arrayed ACT (Fig. 13). [16] An RTF is a kind of an optical finite impulse response filter whose reflection spectrum is determined by reflection-type delay line lengths. [28], [29]. When we see an RTF as a tunable filter, the tuning efficiency for a given refractive index change of delay lines is higher than those of conventional filters such as a distributed Bragg reflector. Therefore, we can obtain a practical tuning range of an RTF even with the EO effect whose refractive index change is ∼1/10 of the carrier effect and thermo-optic effect. In addition to the high tuning efficiency, another feature of an RTF is that we can use multiple channels whose reflection spectra are orthogonal to each other. Thus, an N-channel RTF laser has an N-time covering wavelength range unlike an RTF with a single ACT.

In addition to minimizing a PIC size for a high yield, a narrow pitch between arrayed components is also important for avoiding a long bent waveguide connecting components which cause undesirable excitations of higher-order propagation modes. Unlike a high-speed arrayed modulator-integrated laser [27], usually only one ACT of a tunable laser with an arrayed gain is biased with DC operation. In such a PIC, the ACT pitch is determined in terms of optical decoupling (typically ∼10 μm) rather than thermal and/or electric crosstalk. The pitch corresponds to an over 50 μm ACT-array region of the RTF laser shown in Fig. 13. Thus, if we start the wafer process of the RTF laser, we need a regrowth hard mask with over 50-μm width for the arrayed ACT, resulting in degraded wafer flatness after the regrowth. This makes the wafer process difficult since the RTF laser is a kind of an interferometric PIC that is sensitive to the critical dimension of the waveguide. [29] In addition to control of the critical dimension, the flatness is also important since we use no resin such as Benzocyclobutene for the planarization in the wafer process of the RTF laser to suppress the external stress to the RTF. [30] As is the case in the wafer process of SOA-DP-IQM shown in Fig. 11, we start the wafer process of the laser with the 1st epi with an EO-MQW and partially replace the 1st epi with a 2nd-epi with an optical-gain MQW. The lasing spectra of the five-channel RTF laser and the output power as a function of current to ACT1 are shown in Fig. 14(a) and (b), respectively. The spectra shown in Fig. 14(a) were measured at a bias current of 40 mA for one ACT in five which

corresponds to ∼1 mW as shown in Fig. 14(b). We observed different lasing wavelengths for each biased ACT. The spectra plotted with dashed lines correspond to tuned ones obtained by applying voltages (∼−1.5V) to a coarse tuning electrode for red or blue shift. Each side-mode suppression ratio (SMSR) was over 40 dB. Furthermore, we confirmed a white noise level of ∼70 kHz in frequency noise spectrum measurement for the ACT1 (Fig. 14(c)) when all tuning electrodes were short state (0V), which corresponded to less than 300-kHz laser line width [31]. These results also indicate that we successfully obtained a practically low cavity loss including the excess loss of the PRG boundary.

V. Conclusion

In this paper, we described the newly developed PRG for InP PICs in which a limited area corresponding to a 200-μm waveguide on a 1st passive epi is replaced with a 2nd active epi. Since we can partially add an optical-gain function on a non-stripe-type PIC using the PRG, we can use the same 1st epi regardless of the presence or absence of active functions in an objective PIC. Thus, the developed process makes the wafer process of InP PICs simple, resulting in low cost. We experimentally clarified the allowable dimension of the replaced area in terms of μ-PL qualities. A 200-μm SOA fabricated by using the PRG exhibited optical net gains of larger than 5 dB, which are comparable to those of conventionally reported SOAs. We also showed the practical applications of PRG for an SOA-DP-IQM and EO RTF laser with an ACT array. The former showed over 25-dB ERs in addition to improved insertion losses. Moreover, the latter exhibited SMSRs of over 40 dB and a frequency phase noise spectrum with a ∼70-kHz floor. These results prove the practical quality of multifunctional InP wafers obtained by the PRG.

References

[1] M. Smit *et al.*, “An introduction to InP-based generic integration technology,” *Semicond. Sci. Technol.*, vol. 29, no. 8, 2014, Art. no. 083001.

[2] S. Arafin and L. A. Coldren, “Advanced InP photonic integrated circuits for communication and sensing,” *IEEE J. Sel. Topics Quantum Electron.*, vol. 24, no. 1, Jan.-Feb. 2018, Art. no. 6100612.

[3] A. Himeno, K. Kato, and T. Miya, “Silica-based planar lightwave circuits,” *IEEE J. Sel. Topics Quantum Electron.*, vol. 4, no. 6, pp. 913–924, Nov./Dec. 1998.

[4] C. Doerr *et al.*, “Single-chip silicon photonics 100-Gb/s coherent transceiver,” in *Proc. Opt. Fiber Commun. Conf.*, 2014, pp. 1–3.

[5] S. Yamanaka *et al.*, “Silicon photonics coherent optical subassembly with EO and OE bandwidths of over 50 GHz,” in *Proc. Opt. Fiber Commun. Conf.*, 2020, pp. 1–3.

[6] T. Okimoto *et al.*, ” InP-based butt-joint coupled waveguide photodiodes integrated with various functions for 100 GBaud coherent detection,” *IEEE J. Sel. Topics Quantum Electron.*, vol. 28, no. 2, Mar./Apr. 2022, Art. no. 3801507.

[7] W. Kobayashi *et al.*, “Design and fabrication of 10-/40-Gb/s, uncooled electroabsorption modulator integrated DFB laser with butt-joint structure,” *J. Lightw. Technol.*, vol. 28, no. 1, pp. 164–171, 2010.

[8] Y. Ueda *et al.*, “Low driving voltage operation of MZI-type EA modulator integrated with DFB laser using optical absorption and interferometric extinction,” *IEEE J. Sel. Topics Quantum Electron.*, vol. 21, no. 6, Nov./Dec. 2015, Art. no. 1501306.

[9] S. Kanazawa *et al.*, “Flip-chip interconnection technique for beyond 100-Gb/s (4 × 25.8-Gb/s) EADFB laser array transmitter,” *J. Lightw. Technol.*, vol. 34, no. 2, pp. 296–302, 2016.

[10] T. Shindo *et al.*, “High power and high speed SOA assisted extended reach EADFB laser (AXEL) for 53-Gbaud PAM4 fiber-amplifier-less 60-km optical link,” *J. Lightw. Technol.*, vol. 38, no. 11, pp. 2984–2991, 2020.

[11] S. Kanazawa *et al.*, “High output power SOA assisted extended reach EADFB laser (AXEL) TOSA for 400-Gbit/s 40-km fiber-amplifier-less transmission,” *J. Lightw. Technol.*, vol. 39, no. 4, pp. 1089–1095, 2021.

[12] Y. Ueda *et al.*, “4x4 InAlGaAs/InAlAs optical-switch fabric by cascading Mach–Zehnder interferometer-type optical switches with low-power and low-polarization-dependent operation,” *IEEE Photon. Technol. Lett.*, vol. 24, no. 9, pp. 757–759, May 2012.

[13] N. Kikuchi *et al.*, “80-Gb/s low-driving-voltage InP DQPSK modulator with an n-p-i-n structure,” *IEEE Photon. Technol. Lett.*, vol. 21, no. 12, pp. 787–789, Jun. 2009.

[14] R. A. Griffin, S. K. Jones, N. Whitbread, S. C. Heck, and L. N. Langley, “InP Mach–Zehnder modulator platform for 10/40/100/200-Gb/s operation,” *IEEE J. Sel. Topics Quantum Electron.*, vol. 19, no. 6, pp. 158–166, Nov./Dec. 2013.

[15] Y. Ueda, Y. Ogiso, and N. Kikuchi, “InP PIC technologies for high-performance Mach-Zehnder modulator,” *Proc. SPIE*, 2017, Art. no. 1012905.

[16] Y. Ueda, T. Shindo, S. Kanazawa, N. Fujiwara, and M. Ishikawa, “Electro-optically tunable laser with ultra-low tuning power dissipation and nanosecond-order wavelength switching for coherent networks,” *Optica*, vol. 7, no. 8, pp. 1003–1006, 2020.

[17] R. A. Griffin *et al.*, “InP coherent optical modulator with integrated amplification for high capacity transmission,” in *Proc. Opt. Fiber Commun. Conf.*, 2015, pp. 1–3.

[18] J. S. Roberts, J. P. R. David, L. Smith, and P. L. Tihanyi, “The influence of trimethylindium impurities on the performance of InAlGaAs single quantum well lasers,” *J. Cryst. Growth*, vol. 195, no. 1–4, pp. 668–675, 1998.

[19] M. Aoki *et al.*, “InGaAs/InGaAsP MQW electroabsorption modulator integrated with a DFB laser fabricated by band-gap energy control selective area MOCVD,” *IEEE J. Quantum Electron.*, vol. 29, no. 6, pp. 2088–2096, Jun. 1993.

[20] T. Fujii and M. Ekawa, “Origin of compositional modulation of InGaAs in selective area metalorganic vapor phase epitaxy,” *J. Appl. Phys.*, vol. 78, no. 9, pp. 5373–5386, 1995.

[21] T. Tsuchiya, J. Shimizu, M. Shirai, and M. Aoki, “InGaAlAs selective-area growth on an InP substrate by metalorganic vapor phase epitaxy,” in *Proc. Int. Conf. Indium Phosphide Related Mater.*, 2003, pp. 546–549.

[22] Y. Barbarin, E. A. J. M. Bente, C. Marquet, E. J. S. Leclere, J. J. M. Binsma, and M. K. Smit, “Measurement of reflectivity of butt-joint active-passive interfaces in integrated extended cavity lasers,” *IEEE Photon. Technol. Lett.*, vol. 17, no. 11, pp. 2265–2267, Nov. 2005.

[23] M. L. Nielsen *et al.*, “SOA-booster integrated Mach–Zehnder modulator: Investigation of SOA position,” *J. Lightw. Technol.*, vol. 28, no. 5, pp. 837–846, 2010.

[24] R. Bonk *et al.*, “Impact of alfa-factor on SOA dynamic range for 20 GBd BPSK, QPSK and 16-QAM signals,” in *Proc. Opt. Fiber Commun. Conf./Nat. Fiber Optic Engineers Conf.*, 2011, pp. 1–3.

[25] J. Ozaki *et al.*, “500-Gb/s/λ Operation of ultra-low power and low-temperature-dependence Inp-based high-bandwidth coherent driver modulator,” *J. Lightw. Technol.*, vol. 38, no. 18, pp. 5086–5091, 2020.

[26] Y. Ueda *et al.*, “Compact InP spot-size converter with vertically tapered core layer formed by micro-loading effect,” *IET Electron. Lett.*, vol. 53, no. 12, pp. 797–799, 2017.

[27] T. Fujisawa *et al.*, “Low-loss cascaded Mach–Zehnder multiplexer integrated 25-Gbit/s x 4-Lane EADFB laser array for future CFP4 100 GbE transmitter,” *IEEE J. Quantum Electron.*, vol. 49, no. 12, pp. 1001–1007, Dec. 2013.

[28] Y. Ueda, T. Fujisawa, K. Takahata, M. Kohtoku, and H. Ishii, “InP-based compact transversal filter for monolithically integrated light source array,” *Opt. Express*, vol. 22, no. 7, pp. 7844–7851, 2014.

[29] Y. Ueda, T. Fujisawa, and M. Kohtoku, “Eight-channel reflection-type transversal filter for compact and easy-to-fabricate Inp-based optical multiplexer,” *J. Lightw. Technol.*, vol. 34, no. 11, pp. 2684–2691, 2016.

[30] Y. Ueda, Y. Hashizume, T. Yamada, H. Matsuzaki, and M. Ishikawa, “Theoretical and experimental investigation of external-stress effect on quantum-well-based semiconductor interferometer performance,” *Appl. Phys. Express*, vol. 14, 2021, Art. no. 091005.

[31] S. Camatel and V. Ferrero, “Narrow linewidth CW laser phase noise characterization methods for coherent transmission system applications,” *J. Lightw. Technol.*, vol. 26, no. 17, pp. 3048–3055, 2008.

Yuta Ueda (Member, IEEE) was born in Ogaki, Japan, in 1983. He received the B.E., M.E., and Ph.D. degrees in electrical engineering and bioscience from Waseda University, Shinjuku, Japan, in 2007, 2008, and 2011, respectively. From 2010 to 2011, he was a Research Fellow with the Japan Society for the Promotion of Science. He joined NTT Photonics Laboratories, NTT Corporation, Kanagawa, Japan, in 2011. Since 2020, he has been a Visiting Associate Professor with Kyushu University, Fukuoka, Japan. He is currently with the NTT Device Innovation Center. His current research interests include semiconductor photonic integrated circuits including tunable lasers and modulators for optical communication and remote sensing systems. He is a Member of the Japan Society of Applied Physics (JSAP) and the Institute of Electronics, Information, and Communication Engineers (IEICE) of Japan.

Yusuke Saito was born in Shizuoka, Japan, in 1992. He received the B.S. degrees in applied physics from the Tokyo University of Science, Tokyo, Japan, in 2016, and the M.E. degrees in electrical and electronic engineering from the Tokyo Institute of Technology, Tokyo, Japan, in 2018. He joined NTT Device Innovation Center, Kanagawa, Japan, in 2018. His current research focuses on InP-based photonic integrated devices. He is a Member of the Institute of Electronics, Information, and Communication Engineers (IEICE) of Japan.

Josuke Ozaki was born in Aichi, Japan, in 1986. He received the B.E. and M.E. degrees in engineering science from Osaka University, Osaka, Japan, in 2010 and 2012, respectively. He joined NTT Photonics Laboratories, Kanagawa, Japan, in 2012. His current research focuses on high-speed optical modulators. He is a Member of the Institute of Electronics, Information and Communication Engineers of Japan.

Yoshihiro Ogiso (Member, IEEE) was born in Fukui, Japan, in 1985. He received B.E., M.E., and Ph.D. degrees in applied physics in optoelectronics from Waseda University, Tokyo, Japan, in 2008, 2010, and 2020, respectively. In 2010, he joined NTT Photonics Laboratories, Kanagawa, Japan. He is currently with NTT Device Innovation Center. His research focuses on the development of optical modulators. He is a Member of the IEEE Photonics Society and the Institute of Electronics, Information and Communication Engineers.

Takahiko Shindo (Member, IEEE) received the B.E., M.E., and Ph.D. degrees in electrical and electronic engineering from the Tokyo Institute of Technology, Tokyo, Japan, in 2008, 2010, and 2012, respectively. He was a Research Fellow with the Japan Society for the Promotion of Science. In April 2013, he joined NTT Photonics Laboratories (now NTT Device Innovation Center), NTT Corporation, Kanagawa, Japan, where he is currently engaged in research on optical semiconductor devices. Dr. Shindo is a Member of the IEEE Photonics Society, the Japan Society of Applied Physics (JSAP), and the Institute of Electronics, Information and Communication Engineers (IEICE). He was the recipient of a research fellowship for young scientists from the Japan Society for the Promotion of Science for the years 2010 to 2012.

Yasuaki Hashizume received the B.S. degree in physics from Nagoya University, Aichi, Japan, in 1999, and the Dr. Eng. degree from Kyushu University, Fukuoka, Japan, in 2015. In 1999, he joined NTT Photonics Laboratories, Ibaraki, Japan. Since 1999, he has been involved in the development of planar lightwave circuits. In 2014, he joined the NTT Device Innovation Center, Kanagawa, Japan. He is a Member of the Institute of Electronics, Information, and Communication Engineers of Japan.

Mitsuteru Ishikawa (Member, IEEE) was born in Tochigi, Japan, in 1972. He received the B.E. and M.E. degrees in applied physics from the University of Tokyo, Tokyo, Japan, in 1995 and 1997, respectively. In 1997, he joined NTT Opto-Electronics Laboratories, Kanagawa, Japan. Since then, he has been involved in development and research on semiconductor-based optical devices for WDM optical communication systems. He is a Member of the Japan Society of Applied Physics and the Institute of Electronics, Information, and Communication Engineers of Japan.